Spatiotemporal Energy Partitioning in a Nonthermally Dominated Two-loop Solar Flare

Galina G. Motorina[1,2,3] , Gregory D. Fleishman[4] , and Eduard P. Kontar[5]
[1] Astronomical Institute of the Czech Academy of Sciences, 251 65 Ondřejov, Czech Republic; galina.motorina@asu.cas.cz
[2] Central Astronomical Observatory at Pulkovo of Russian Academy of Sciences, St. Petersburg, 196140, Russia
[3] Ioffe Institute, Polytekhnicheskaya, 26, St. Petersburg, 194021, Russia
[4] Center for Solar-Terrestrial Research, New Jersey Institute of Technology, Newark, NJ 07102, USA
[5] School of Physics & Astronomy, University of Glasgow, Glasgow G12 8QQ, UK

Abstract

Solar flares show remarkable variety in the energy partitioning between thermal and nonthermal components. Those with a prominent nonthermal component but only a modest thermal one are particularly well suited for study of the direct effect of the nonthermal electrons on plasma heating. Here, we analyze such a well-observed, impulsive single-spike nonthermal event, a solar flare SOL2013-11-05T035054, where the plasma heating can be entirely attributed to the energy losses of these impulsively accelerated electrons. Evolution of the energy budget of thermal and nonthermal components during the flare is analyzed using X-ray, microwave, and EUV observations and three-dimensional modeling. The results suggest that (i) the flare geometry is consistent with a two-loop morphology and the magnetic energy is likely released due to interaction between these two loops; (ii) the released magnetic energy is converted to the nonthermal energy of accelerated electrons only, which is subsequently converted to the thermal energy of the plasma; (iii) the energy is partitioned in these two flaring loops in comparable amounts; (iv) one of these flaring loops remained relatively tenuous but rather hot, while the other remained relatively cool but denser than the first. Therefore, this solar flare demonstrates an extreme efficiency of conversion of the free magnetic energy to the nonthermal energy of particle acceleration and the flow of energy into two loops from the nonthermal component to the thermal one with negligible direct heating.

Unified Astronomy Thesaurus concepts: Solar flares (1496); The Sun (1693); Solar extreme ultraviolet emission (1493); Solar radio emission (1522); Solar x-ray emission (1536)

Supporting material: animation

1. Introduction

Magnetic energy accumulated in the solar atmosphere over days can be sporadically promptly released on a timescale of minutes to produce a solar flare—a transient brightening observed across virtually the whole electromagnetic radiation spectrum from radio to gamma-rays. The current understanding of solar flares (e.g., Holman et al. 2011, as a review) suggests that the primary energy release due to magnetic reconnection produces a downward beam of accelerated electrons. These energetic electrons generate nonthermal microwave gyrosynchrotron radiation in the ambient magnetic field and hard X-ray (HXR) emission in interactions with ambient particles. These collisions with plasma result in heating of the coronal plasma and dense chromospheric layers, stimulating evaporation of the heated chromospheric plasma into the coronal portion of the flaring loop(s). Finally, the hot plasma cools down due to conductive and radiative losses, whose signatures are routinely observed at soft X-ray (SXR) and ultraviolet (UV) wavelengths.

The close causal relationship between nonthermal emissions, produced by accelerated particles, and thermal emissions, produced by the plasma that is heated during the flare and cools down after the energy release, is one of the major ingredients in the standard model of a solar flare (CSHKP: Carmichael 1964; Sturrock 1966; Hirayama 1974; Kopp & Pneuman 1976; Shibata et al. 1995; Tsuneta 1997; Shibata 1999). Such a casual relationship, known as the Neupert effect (Neupert 1968), is often observed in flares (Datlowe 1975; Dennis & Zarro 1993; Sylwester et al. 1993; McTiernan et al. 1999). In

many cases, however, the Neupert effect is not observed (Dennis & Zarro 1993; Veronig et al. 2005; Su et al. 2008; Battaglia et al. 2009), which indicates richer physics of plasma heating than the simple physics of Coulomb collisional loss by nonthermal particles.

Accordingly, a number of physical mechanisms for "direct" heating of coronal plasma have been proposed, such as adiabatic heating due to Fermi (Miller et al. 1990; Chupp 1996; Dahlin et al. 2017) and betatron mechanisms (Sakurai 1965; Brown & Hoyng 1975; Somov 1979; Bogachev & Somov 2005; Grady et al. 2012), due to a reconnecting current sheet located at the apex of the magnetic cusp, due to shock waves associated with the outflow of plasma from the current sheet (see, e.g., Priest & Forbes 2002), or due to strong electric fields that might be produced by the Rayleigh–Taylor instability (Stepanov & Zaitsev 2016; Zaitsev & Stepanov 2017). In addition, the heat transport is likely to be complicated by non-local effects due to electrostatic, magnetostatic, and/or electromagnetic turbulence (Somov 1979; Jakimiec & Fludra 1991; Jakimiec et al. 1998; Bian et al. 2016).

As a result, the partitions between the thermal and nonthermal energies vary over an extremely broad range in solar flares—from entirely thermal (Dennis 1985; Gary & Hurford 1989; Altyntsev et al. 2012; Fleishman et al. 2015) to essentially nonthermal (Dennis 1985; Bastian et al. 2007; Krucker et al. 2010; Fleishman et al. 2011). In spite of this variety of thermal-to-nonthermal energy ratios, the flare magnitude is commonly characterized by SXR class based on the flux of the thermal SXR emission. Should the thermal SXR flux be somewhat low, the flare is deemed weak even though it

may contain a strong nonthermal component, which, in some cases, can be dominant in the flare energy budget.

Intuitively, such nonthermal-dominated events should demonstrate the Neupert effect; however, the converse is not necessarily true: the presence of the Neupert effect does not guarantee the dominance of the nonthermal energy in the flare. For example, Veronig et al. (2005) found that the correlations between physical values of the thermal and nonthermal energies were lower than correlations between phenomenologically defined thermal and nonthermal emissions, which was interpreted as evidence of additional "direct" plasma heating. Thus, the nonthermal-dominated flares likely represent only a subset of impulsive flares showing the Neupert effect. The critical obstacle in determining nonthermal energy and hence the flare power is related to poorly known low-energy cutoff in the energy spectrum of accelerated particles. The low-energy cutoff problem arises because the low-energy part of the electron spectrum is often masked by bright thermal emission. Thus, this low-energy part of the nonthermal electron spectrum could be much better studied in flares with anomalously weak thermal response than in a "normal" flare. In addition, recent development of the warm-target model allowed Kontar et al. (2019) to obtain the low-energy electron cutoff with $\sim$7% statistical uncertainty at the 3σ level for a selected flare, hence allowing quantitative studies of the nonthermal energetics in solar flares.

For nonthermal electron analysis, it is advantageous to use the nonthermal-dominated events out of those that do not show any appreciable preflare heating but demonstrate a prominent impulsive nonthermal phase that is followed by thermal emission; these are called "early impulsive flares" (Feldman et al. 1994; Sui et al. 2007). It has recently been recognized that some early impulsive flares (White et al. 1992; Bastian et al. 2007; Fleishman et al. 2011, 2016; Masuda et al. 2013) have only a very small thermal plasma response so that these events are often even not listed as *Geostationary Operational Environmental Satellite* (*GOES*) flares. For that reason, they were classified as "cold" flares (Lysenko et al. 2018). However, the 2002 July 30 "cold" flare reported by Fleishman et al. (2011) is a tenuous flare with a thermal number density not exceeding $2 \times 10^9 \, \mathrm{cm}^{-3}$ in the coronal part of the flaring loop. Therefore, the thermal SXR emission is low because the emission measure is low, although the temperature can in fact be rather high. In contrast, two other cold flares reported by Bastian et al. (2007) and Masuda et al. (2013) were dense, with a thermal number density in excess of $10^{11} \, \mathrm{cm}^{-3}$. In such cases, the fast particle losses in the coronal part of the loop are large and the increase in thermal energy is relatively strong; but, because of the high density, the net temperature increase, and hence the SXR emission, is rather modest. However, previous studies of such events do not provide a comprehensive picture of energy assessment due to the weak thermal component being poorly constrained by *GOES* observations only (Bastian et al. 2007; Fleishman et al. 2011, 2016).

Recently, a statistical study of "cold" flares has been performed by Lysenko et al. (2018) for the period from 1994 to 2017, with 27 selected events, where the authors classified such events as short and hard flares, which are typically produced in compact structures (likely, short flaring loops) with a strong magnetic field, stronger than that of "normal" flares. Lysenko et al. (2018) proposed that these "cold" flares may offer a rather clean case for studying thermal plasma heating in

response to the nonthermal electron acceleration in flares. Indeed, for such events the spatially resolved evolution of thermal energy can be quantified in detail using EUV data, since in the case of relatively modest plasma heating, the EUV images are not affected by saturation and the flare plasma temperature is expected to be in the range to which *Solar Dynamics Observatory*/Atmospheric Imaging Assembly (*SDO*/AIA) is most sensitive. Thus, *SDO*/AIA observations are much better suited to quantifying the thermal component than spatially unresolved *GOES* data employed so far (Bastian et al. 2007; Battaglia et al. 2015, 2019; Fleishman et al. 2016; Lysenko et al. 2018).

The present paper is focused on one of the events (SOL2013-11-05T035054) from the list of Lysenko et al. (2018), which was well observed with imaging and spectroscopic instruments. Here, for the first time, we employ a detailed analysis of EUV data from *SDO*/AIA to quantify the moderately heated component of the flare plasma, while using *Reuven Ramaty High Energy Solar Spectroscopic Imager* (*RHESSI*) data to quantify the nonthermal component along with the hot component of the flaring plasma. Combining these data with three-dimensional (3D) modeling based on *SDO*/HMI vector magnetogram and nonlinear force-free field (NLFFF) reconstruction, we devise a 3D model of this flare and validate it by comparison with X-ray and microwave data. This analysis reveals two distinct flaring loops, one of which is indeed relatively cold, $\lesssim$10 MK. The other one, however, is rather hot, with a temperature up to $\sim$30 MK during the impulsive phase. Furthermore, the evolution of the spatially resolved thermal energy is governed by the nonthermal component of the flare. We found that the evolution of thermal energy is quantitatively consistent with the rate of nonthermal energy deposition; thus, here we do have a case where the flare energy goes primarily into particle acceleration, while the observed plasma heating is entirely accounted for by dissipation of this nonthermal energy; there is no room for any statistically significant additional "direct" plasma heating in this event.

2. Observations

Solar flare SOL2013-11-05T035054 occurred at active region AR 11890 at 03:48:40 UT with the position ($-771''$, $-250''$) in heliocentric coordinates, localized by the Nobeyama RadioHeliograph (NoRH) (Table 1 of Lysenko et al. 2018). It demonstrated an impulsive HXR peak at energies above 12 keV that reached a maximum at $\sim$03:50:25 UT, with a smoother peak at lower energies that reached a maximum at 03:50:54 UT and ended at 03:56:40 UT based on the *RHESSI* observations. The flare was included in the list of early impulsive "cold" flares studied by Lysenko et al. (2018), who analyzed SXR, HXR, and microwave emission, observed with *GOES* (White et al. 2005), Konus–*Wind* (Aptekar et al. 1995; Pal'shin et al. 2014), Nobeyama Radio Polarimeters (NoRP, Torii et al. 1979), Radio Solar Telescope Network (RSTN, Guidice et al. 1981), and Solar Radio Spectropolarimeters (SRS, Muratov 2011). Here, for a detailed case study of the flare SOL2013-11-05T035054 we additionally employ data from *RHESSI* (Lin et al. 2002), which provides images with an angular resolution of a few arcseconds and photon spectra at energies from $\sim$3 keV to 17 MeV with modest temporal resolution (4 s). We also use data obtained with *SDO*/AIA (Lemen et al. 2012) to more accurately quantify thermal and nonthermal energies of the solar flare.
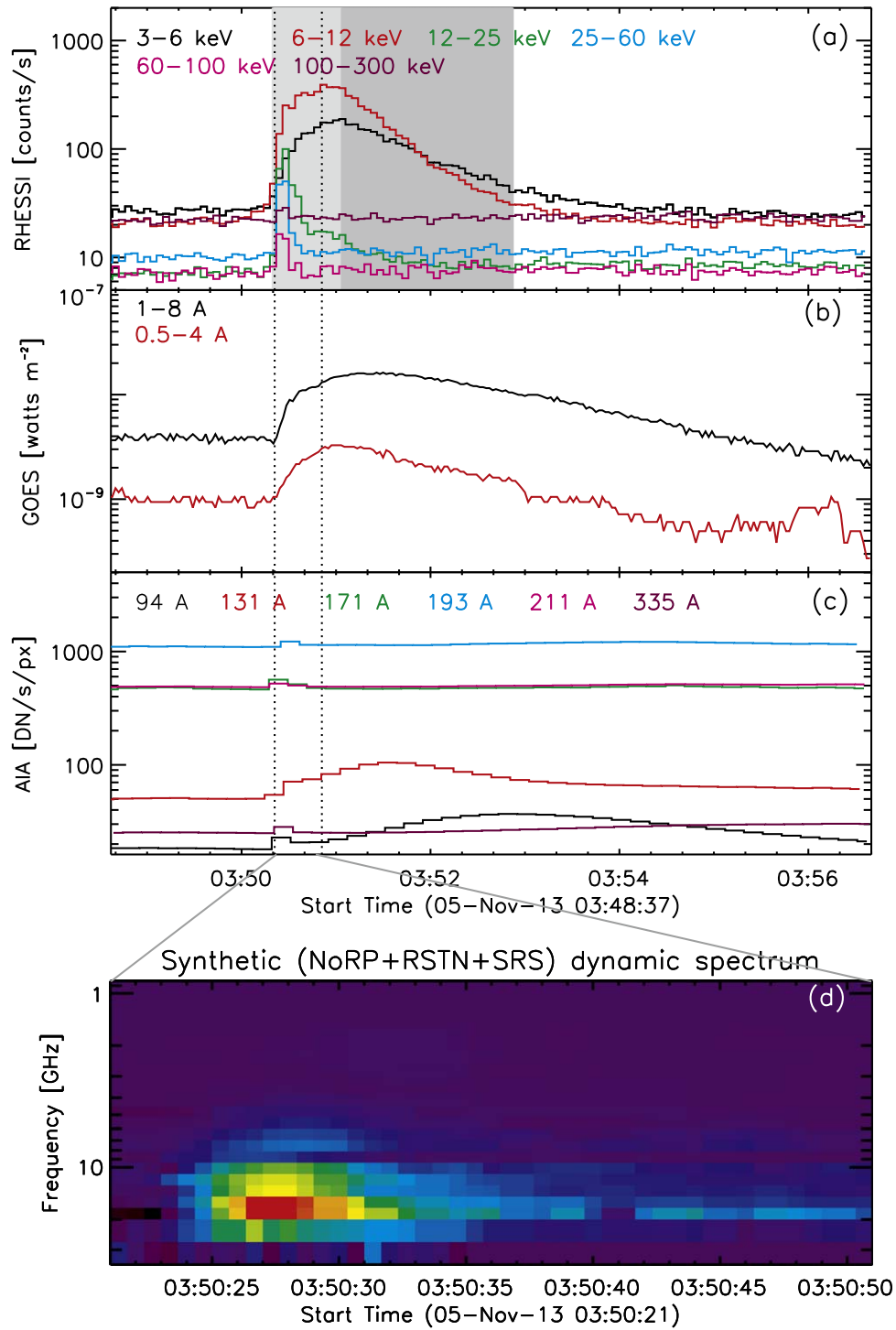
Figure 1. Overview of the 2013 November 5 flare. (a) *RHESSI* light curves; (b) *GOES* light curves: to highlight the flare-associated flux in the 1–8 Å light curve, we subtracted a substantial fraction, 8×10^{-7} [W m^{-2}], of the preflare background; (c) the AIA light curves obtained from the selected FOV (see Figure 2); (d) NoRP +RSTN+SRS dynamic spectrum (the absolute peak of the radio flux density is 318 sfu) of the impulsive flare phase. Vertical dotted lines indicate the impulsive phase shown in the bottom panel. The light gray area shows the 4 s fitted time intervals and the dark gray area shows the 12 s fitted time intervals of the *RHESSI* observations.

The flare has a short impulsive phase, ∼15 s, prominently seen in the nonthermal microwave and HXR emissions, followed by a ∼3 minute gradual phase, thus clearly showing the Neupert effect (Neupert 1968). The flare produced strong impulsive emission in the HXR (up to 300 keV), microwave, and EUV wavelength domains, seen respectively by *RHESSI* and Konus–*Wind*, by NoRP, RSTN, and SRS, and by

SDO/AIA at ∼03:50:20 UT, while a very modest SXR enhancement. Figure 1 shows (a) *RHESSI* and (b) *GOES* light curves, (c) EUV light curves integrated over the field of view (FOV) shown below in Figure 2 obtained with *SDO*/AIA, and (d) a synthetic microwave spectrum combining the data of the impulsive flare phase obtained with NoRP, RSTN, and SRS. The radio spectral peak frequency was unusually high
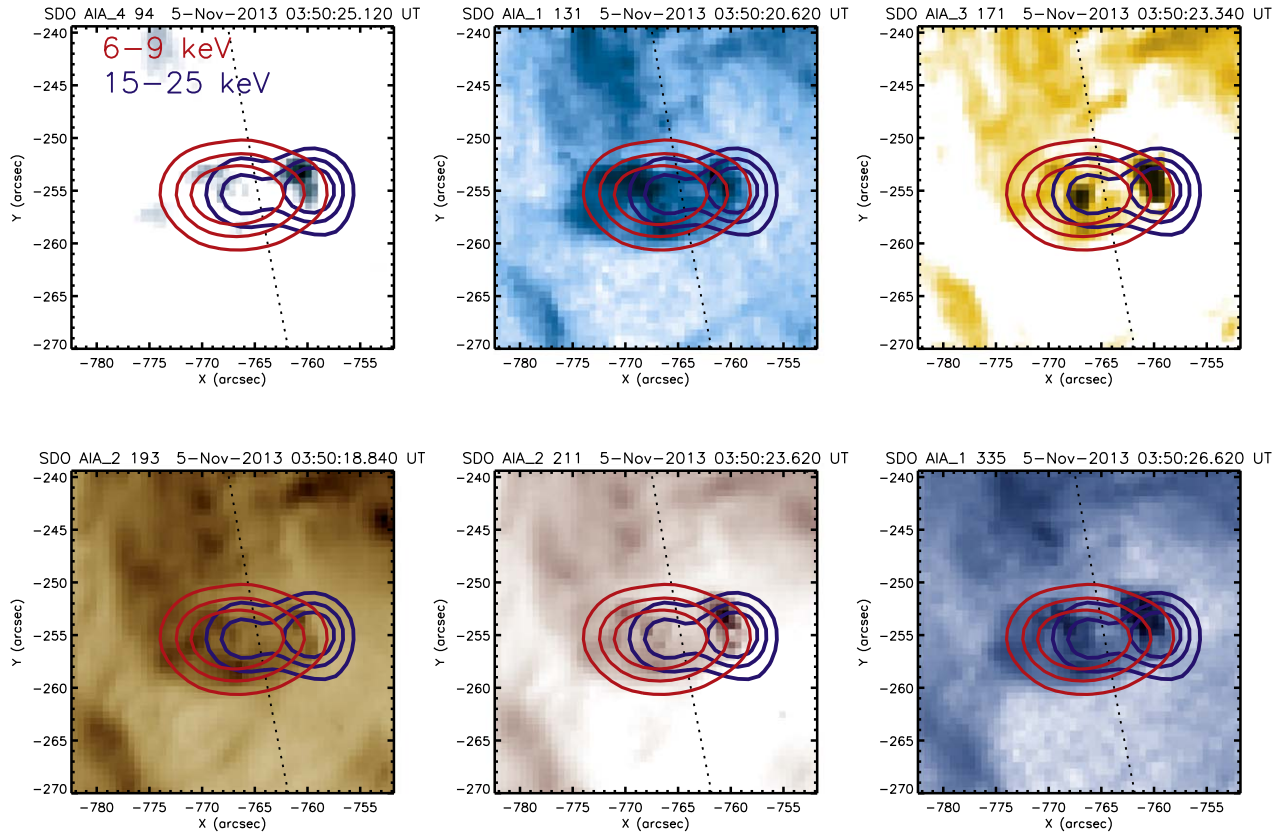
Figure 2. AIA maps of the 2013 November 5 flare with overlaid *RHESSI* CLEAN image (clean beam width factor is CBWF = 1.8) 30%, 50%, and 70% contours for 6–9 keV (red lines) and 15–25 keV (blue lines) for time interval 03:50:20–03:50:40 UT. For coalignment of the *RHESSI* and AIA maps, the AIA roll angle has been selected to be AIA_roll_angle = 0.11.

($\sim$20 GHz) and the microwave burst was very short ($\sim$15 s), which indicates a reasonable compactness of the flare source. The *SDO*/AIA images were not saturated during the entire flare despite the presence of nonthermal emission up to 300 keV. The maximum of X-ray emission for $E > 12$ keV and the microwave emission occur simultaneously with bumps in the EUV light curves at $\sim$03:50:25 UT, while EUV peaks at 94, 171, 193, 211, and 335 Å indicate an impulsive heating process for low temperatures ($\log_{10}(T/K) \sim 5.5$–6.8) and the subsequent cooling. In summary, the described flare had a single impulsive peak followed by a reasonably simple, modest thermal response, and it can be considered as an "elementary" energy release/acceleration episode.

2.1. EUV and X-Ray Imaging with AIA and RHESSI

SDO/AIA observations provide the EUV images of the full solar disk with $\sim$1″5 spatial and 12 s temporal resolution in several wavebands. In this study only six EUV wavebands (94, 131, 171, 193, 211, 335 Å) are used, which are sensitive to emission of a coronal flare plasma. The AIA images additionally calibrated with aia_prep.pro and normalized by the exposure time in six EUV wavebands were taken every 12 s during the time interval between 03:48:37 and 03:56:40 UT. There was no saturation of the AIA data during the flare. To analyze the EUV data we choose a square region that fully encloses the flare emission over the entire course of the flare (see the FOV shown in Figure 2). The AIA Data Numbers were inferred from that FOV, which will be further investigated in Section 2.3.

Figure 2 also shows the *RHESSI* CLEAN image as 30%, 50%, and 70% contours for 6–9 keV and 15–25 keV for the time interval 03:50:20–03:50:40 UT. To co-align the AIA and *RHESSI* observations the AIA maps were rotated (AIA_roll_angle = 0.11) due to probable roll-angle calibration error in one of the instruments, as shown earlier by Battaglia & Kontar (2011) and further discussed by Kuhar et al. (2016). The AIA images at 94 and 171 Å display double footpoints that lie inside the HXR contours. This likely indicates the existence of two connecting loops in the horizontal direction. Loop–loop interactions have been proposed by Tajima et al. (1987) and Hanaoka (1999) to drive energy release in solar flares with multi-loop morphology; this scenario is further supported by simulations of loop–loop interaction (Kašparová et al. 2005) and numerous observations of two-loop flare configurations (e.g., Fleishman et al. 2016; Altyntsev et al. 2019).

To determine the thermal and nonthermal X-ray sources, the *RHESSI* CLEAN (Hurford et al. 2002) images for 6–9 keV and 15–25 keV with clean width beam factor CBWF = 1.8 (see Kontar et al. 2010) were made using detectors 3–8 with $\sim$6″79 nominal spatial resolution for the time interval 03:50:20–03:50:40 UT, which corresponds to the HXR impulsive peak (Figure 2, see Section 2.3.1).

2.2. X-Ray Diagnostics with RHESSI and Konus–Wind

To analyze the nonthermal properties of the flare, we employ spectral analysis in the X-ray domain. The *RHESSI* data with appropriately subtracted background were fitted with two models: (i) an isothermal plus collisional thick-target model
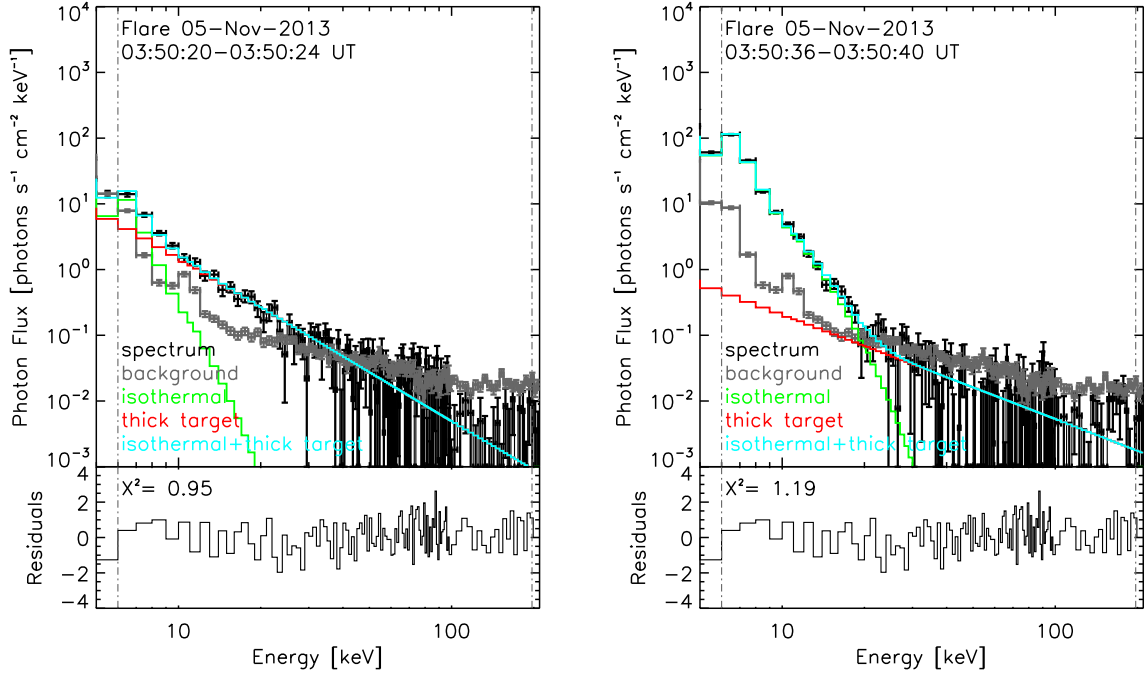
Figure 3. Examples of the *RHESSI* fits (light blue histogram) with the isothermal (green histogram) plus thick-target model (red histogram) during the nonthermal peak at 03:50:20–03:50:24 UT (left panel) and a few seconds later at 03:50:36–03:50:40 UT (right panel). The *RHESSI* data and the background level are shown with black and gray histograms respectively. The bottom panels indicate residuals.
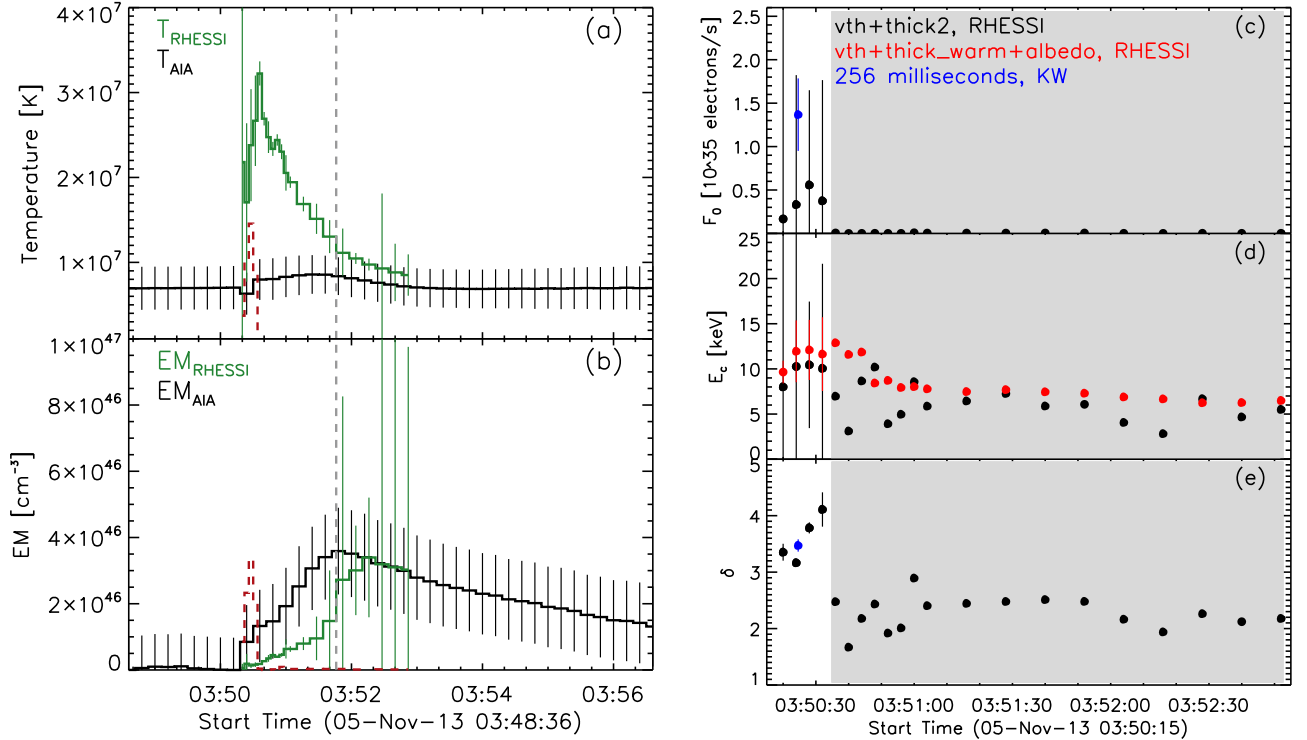

Figure 4. Time evolution of (a) *T*, (b) emission measure (EM), and (c)–(e) nonthermal parameters for the 2013 November 5 flare. (a) *RHESSI* temperature (green histogram) from the isothermal model for spatially unresolved full solar disk and AIA temperature (black histogram) from the FOV shown in Figure 2. (b) *RHESSI* (green histogram) and preflare-subtracted AIA (black histogram) emission measure inferred as described for the upper panel. The vertical dashed line indicates the time 03:51:46 UT, when EM and *T* from the *RHESSI* and the AIA data converge. The red dashed histogram indicates the change of *RHESSI* nonthermal energy with time $dW_{\mathrm{nonth}}^{\mathrm{RHESSI}}/dt$ [arbitrary units] (see Equation (6)). (c) Total integrated electron flux F_0, (d) low-energy cutoff E_c, and (e) spectral index δ obtained from the *RHESSI* isothermal + thick-target (black circles), isothermal + warm target + albedo (red circles), and the Konus–Wind fits (blue circles). Vertical lines indicate the range of 1σ error on the fits of the *RHESSI* and the Konus–Wind data. The gray shaded area indicates the time range over which no nonthermal component could be confidently identified in the data.

and (ii) an isothermal plus warm-target model using OSPEX.[6] These fits were applied every 4 s from 03:50:20 UT to 03:51:04 UT because this interval is of the greatest interest, and every 12 s for the interval 03:51:04–03:52:52 UT (the intervals are respectively highlighted by the light and dark gray areas in Figure 1(a)), when the signal in the low-energy (thermal) channels was much higher than the background. Two examples of the *RHESSI* fits are shown in Figure 3, which illustrates a transition from a nonthermal-dominated phase (left panel) to a thermal-dominated one (right panel) a few seconds after the HXR peak at ∼03:50:20 UT. Starting ∼03:50:36 UT, the nonthermal component drops below the background and the thermal component starts to dominate. The time evolution of the fit parameters is shown in Figure 4: the temperature $T_{\rm RHESSI}$ (a), the emission measure $EM_{\rm RHESSI}$ (b), the total integrated electron flux F_0 [in units of 10^{35} electrons s^{-1}] (c), the low-energy cutoff E_c [keV] (d), and the spectral index δ of the electron distribution function above E_c (e).

It is important to emphasize here that the physical meaning of the low-energy cutoff fit parameter E_c is different in the cold-target and warm-target models: it gives only an upper limit to the "true" value of the low-energy cutoff in the spectrum of the nonthermal electrons in the case of a cold target, while it yields the most likely (mean) value in the case of the warm-target model (Kontar et al. 2019), given the adopted parameters of the coronal flaring loop. It is remarkable, however, that for this flare the upper limits (black symbols in panel (d)) and the mean values (red symbols in panel (d)) perfectly match each other within the statistical uncertainties; thus, the upper limits can safely be used as a proxy for E_c. This is important because other warm-target fit parameters (not shown in the figure) come with larger uncertainties than the thick-target parameters. Thus, in what follows we employ the better constrained parameters of the cold thick-target fit.

In addition, to probe whether any fast, sub-second dynamics of the nonthermal component is present, we employed the X-ray data obtained with Konus–*Wind* (Aptekar et al. 1995; Pal'shin et al. 2014). Given that Konus–*Wind* uses triggering and an adaptive spectrum accumulation scheme, only four spectra with 64 ms temporal resolution were available for the 2013 November 5 flare for the time interval 03:50:24.587–03:50:24.843 UT during the rise of the impulsive phase. We fitted the Konus–*Wind* data with the isothermal plus thick-target model, where thermal parameters were taken from the *RHESSI* fit and fixed because Konus–*Wind* registers photons in energy channels above ∼20 keV and thus is insensitive to thermal flaring plasma. The low-energy cutoff E_c = 10.26 keV was taken from values obtained from the *RHESSI* thick-target fit for the same time interval 03:50:24–03:50:28 UT. This fit does not reveal any significant time variability on the scale of ∼100 ms. Therefore, we added up all four spectra and fitted this cumulative Konus–*Wind* spectrum to cross-check the results of the *RHESSI* fit. The total integrated electron flux and spectral index from the Konus–*Wind* fit are shown in Figures 4(c) and (e) (blue circles) and are consistent with the fit parameters obtained from the *RHESSI* data.

2.3. Thermal Plasma Diagnostics with SDO/AIA

2.3.1. Diagnostics Using the Regularized DEMs

To better quantify the thermal properties of the SOL2013-11-05T035054 flare, the observations of the *SDO*/AIA were employed. We note that *SDO*/AIA is only weakly sensitive to plasma much hotter than 10 MK (Motorina & Kontar 2015; Battaglia et al. 2019) and also has a gap in sensitivity around 5 MK; thus, we are only going to employ the AIA data to quantify the relatively cool component (∼10 MK) of the "cold" flare plasma in addition to the much hotter component (∼20–30 MK) already quantified with the *RHESSI* data. We also note that various methods of reconstructing differential emission measures (DEMs) from the AIA data, or even the same method with different settings, may yield dissimilar DEM distributions; however, the moments computed from these distributions (i.e., emission measure and temperature) are more robust than the DEMs themselves. Therefore, we will focus on these integral parameters—emission measure $EM_{\rm AIA}$ [cm^{-3}] and mean temperature $\langle T_{\rm AIA} \rangle$ [K].

To estimate these integral plasma parameters from the AIA FOV with area A [cm^2] (see Figure 2), we determined the DEM $\xi(T)$ [cm^{-5} K^{-1}] in the temperature range 0.5–25 MK using a regularization technique applied to the entire FOV for the AIA data (Hannah & Kontar 2012). The total emission measure from the AIA FOV can be computed as

$$EM_{\rm AIA} = A \int_{T_{\rm min}}^{T_{\rm max}} \xi(T) dT \approx A \sum_i \xi_i(T_i) \Delta T_i \quad (1)$$

and then the mean temperature as

$$\langle T_{\rm AIA} \rangle = \frac{\int_{T_{\rm min}}^{T_{\rm max}} T\xi(T) dT}{\int_{T_{\rm min}}^{T_{\rm max}} \xi(T) dT} \approx \frac{\sum_i T\xi_i(T_i) \Delta T_i}{\sum_i \xi_i(T_i) \Delta T_i}. \quad (2)$$

Figures 4(a) and (b) show the evolution of $\langle T_{\rm AIA} \rangle$ and $EM_{\rm AIA}$ with the minimum preflare emission measure subtracted. After the HXR impulsive peak, the emission measure and temperature both increase; however, the values obtained, from *RHESSI* and *SDO*/AIA respectively, differ. The two instruments are sensitive to different temperature ranges and thus see different sources within the flaring region until ∼03:51:46 UT. After that, both T and EM obtained from *RHESSI* and *SDO*/AIA converge, which likely indicates that the originally hotter plasma component, initially observed with *RHESSI*, has cooled down with time and became undetectable. Finally, in the late decay phase, *RHESSI* becomes insensitive to the cooling plasma and only AIA can fully observe the decay phase of the flare.

2.3.2. Diagnostics Using the Regularized DEM Maps

The spatially resolved AIA data offer a much more detailed diagnostics of the thermal plasma than that performed above in Section 2.3.1. To this end, the same AIA data set (see Section 2.3.1) was used to yield the spatial emission measure $EM_{ij}^{\rm AIA}$ and the mean temperature $\langle T_{ij}^{\rm AIA} \rangle$ of each pixel with coordinates $i = 0, ..., N_{\rm px} - 1$ and $j = 0, ..., N_{\rm px} - 1$, where the number of pixels along each dimension is $N_{\rm px} = 51$ in our case, based on the regularized inversion code developed by Hannah & Kontar (2012, 2013). Because it attempts to solve an ill-posed problem, this algorithm can occasionally give

alternating values, unless the DEMs have been forced to be positive. We checked that this does not typically happen within our flaring region, but occurs mainly in some non-flaring pixels within the FOV; thus, we made the inversion without forcing DEMs to be positive. We found that negative values can occasionally appear at high temperatures, $T > 25\,\mathrm{MK}$, to which AIA is almost insensitive. For this reason, we restrict the range of the employed temperatures to 0.5–25 MK as in Section 2.3.1 (in contrast to the default 0.5–32 MK range).

Then, to subtract the non-flaring foreground and background plasma along each line of sight (LOS), we formed, for each pixel, the averaged distribution $\xi_{ij}^{\mathrm{bk}}(T_k)$ for nine first time intervals that correspond to the preflare phase (03:48:30–03:50:18 UT). This background DEM distribution $\xi_{ij}^{\mathrm{bk}}(T_k)$ was then subtracted from $\xi_{ij}(T_k)$ to form the DEM $\xi_{ij}^{\mathrm{fl}}(T_k)$, which pertains to the flare loops only. Note that AIA has a gap in sensitivity to intermediate plasma temperatures of about 5 MK; for that reason some of the background DEMs $\xi_{ij}^{\mathrm{bk}}(T_k)$ in this temperature range can happen to be larger than $\xi_{ij}(T_k)$, which might yield some negative $\xi_{ij}^{\mathrm{fl}}(T_k)$ values. To ensure that the flaring DEMs $\xi_{ij}^{\mathrm{fl}}(T_k)$ are positively defined, which is essential for further quantitative analysis, any negative values obtained were set to zero. This is justified by the fact that those negative values are always consistent with being zero within their errors. Now, the $\mathrm{EM}_{ij}^{\mathrm{AIA}}$ and $\langle T_{ij}^{\mathrm{AIA}} \rangle$ maps for the flaring DEMs can be calculated similar to Equations (1) and (2):

$$\mathrm{EM}_{ij}^{\mathrm{AIA}} = S_{\mathrm{px}} \int_{T_{\min}}^{T_{\max}} \xi_{ij}^{\mathrm{fl}}(T)\,dT, \qquad (3)$$

$$\langle T_{ij}^{\mathrm{AIA}} \rangle = \frac{\int_{T_{\min}}^{T_{\max}} T\xi_{ij}^{\mathrm{fl}}(T)\,dT}{\int_{T_{\min}}^{T_{\max}} \xi_{ij}^{\mathrm{fl}}(T)\,dT}, \qquad (4)$$

where S_{px} [cm^2] is the area of the AIA pixel. The thermal energy density w_{ij}^{AIA} inferred for the FOV of interest (see Figure 2) can then be defined as

$$w_{ij}^{\mathrm{AIA}} = 3k_{\mathrm{B}}\langle T_{ij}^{\mathrm{AIA}} \rangle \sqrt{\mathrm{EM}_{ij}^{\mathrm{AIA}}/(S_{\mathrm{px}}l_{\mathrm{depth}})} \quad [\mathrm{erg\ cm}^{-3}], \quad (5)$$

where $l_{\mathrm{depth}} = d_{\mathrm{depth}} \times 0.6 \times 7.25 \times 10^7$ [cm] is the adopted length along the LOS taken equal to the mean loop width $d_{\mathrm{depth}} = d_{\mathrm{width}} = 4$ [px] and k_{B} is the Boltzmann constant; both electron and ion contributions are accounted for by using the factor of 3. The value d_{width} is the estimate of the loop width, which we found from inspection of the energy density images shown in Figure 5. The animated Figure 5 shows the time evolution of the temperature $\langle T_{ij}^{\mathrm{AIA}} \rangle$ (top left panel), the emission measure $\mathrm{EM}_{ij}^{\mathrm{AIA}}$ (top right panel), chi-square ($\chi^2 < 2$, bottom left panel), and the thermal energy density w_{ij}^{AIA} (bottom right panel) from the area A. We inferred these parameters for all times during the flare; the reference image in Figure 5 shows the 13th time interval (03:51:06–03:51:18 UT). It is clearly seen that the mean temperature is concentrated around 10 MK during the flare, while the emission measure and the thermal energy density change dramatically and have a peak just after the nonthermal HXR peak time with a decrease thereafter, prominently showing the Neupert effect.

2.4. Energy Budget

Now we have all inputs needed to quantify the thermal-to-nonthermal energy budget in this flare as completely as possible with the available data. The nonthermal energy $W_{\mathrm{nonth}}^{\mathrm{RHESSI}}$ deposited in the flaring volume during the impulsive phase versus time was computed as a cumulative sum using the parameters from the *RHESSI* fits:

$$W_{\mathrm{nonth}}^{\mathrm{RHESSI}} = \int_{-\infty}^{t} F_0 E_c \frac{\delta - 1}{\delta - 2}\,dt \quad [\mathrm{erg}], \qquad (6)$$

where F_0, E_c, and δ are the thick-target parameters (see Section 2.2) from the fitting of the *RHESSI* data displayed in Figures 4(c)–(e); $W_{\mathrm{nonth}}^{\mathrm{RHESSI}}$ is shown in blue in Figure 6.

The associated thermal energy can be computed from both the *RHESSI* and AIA data. To calculate the thermal energy detected by *RHESSI*, we employ the emission measure and temperature obtained from the *RHESSI* fit (see Section 2.2 and Figure 4):

$$W_{\mathrm{therm}}^{\mathrm{RHESSI}} = 3k_{\mathrm{B}}T_{\mathrm{RHESSI}}\sqrt{\mathrm{EM}_{\mathrm{RHESSI}} \times V} \quad [\mathrm{erg}], \qquad (7)$$

where V is the volume of the corresponding thermal source, which is unavailable given that the source is only barely resolved by *RHESSI*. Here we assume that the volume of the *RHESSI* thermal source is comparable to that of the AIA thermal source, which can be evaluated much more precisely. We then justify this assumption a posteriori using 3D modeling (Section 3).

The volume of the AIA thermal source can be estimated as

$$V = S_{\mathrm{eff}} \times l_{\mathrm{depth}} \quad [\mathrm{cm}^3], \qquad (8)$$

where the effective area is defined using the map of the thermal energy density w_{ij}^{AIA} determined in Section 2.3.2 as

$$S_{\mathrm{eff}} = \frac{\left(S_{\mathrm{px}}\sum_{i=1}^{N_{\mathrm{px}}}\sum_{j=1}^{N_{\mathrm{px}}}w_{ij}^{\mathrm{AIA}}\right)^2}{S_{\mathrm{px}}\sum_{i=1}^{N_{\mathrm{px}}}\sum_{j=1}^{N_{\mathrm{px}}}(w_{ij}^{\mathrm{AIA}})^2} \quad [\mathrm{cm}^2]. \qquad (9)$$

This estimate of the volume V is only applicable during the course of the flare, not for the preflare phase. The evolution of the thermal energy $W_{\mathrm{therm}}^{\mathrm{RHESSI}}$ derived from the parameters of the *RHESSI* data fits using Equation (7) is shown in green in Figure 6.

The total thermal energy in the FOV derived from the AIA data is computed from the spatial distribution of the thermal energy density w_{ij}^{AIA}, obtained from the regularized DEM maps, by adding up the contributions from all pixels in the FOV:

$$W_{\mathrm{therm}}^{\mathrm{AIA}} = S_{\mathrm{px}}l_{\mathrm{depth}}\sum_{i=1}^{N_{\mathrm{px}}}\sum_{j=1}^{N_{\mathrm{px}}}w_{ij}^{\mathrm{AIA}} \quad [\mathrm{erg}], \qquad (10)$$

and then subtracting the minimal preflare value $W_{\mathrm{therm,min}}^{\mathrm{AIA}} = 6.35 \times 10^{27}$ [erg], which comes from the non-flaring pixels in the FOV. The evolution of the AIA-derived thermal energy $W_{\mathrm{therm}}^{\mathrm{AIA}}$ is shown in black in Figure 6.

In agreement with our conclusions drawn in Section 2.3.1 (see Figure 4), the evolution of the thermal energy can be subdivided into two stages. In the first stage lasting roughly up to ~03:51:46 UT, *RHESSI* and AIA see two distinct thermal sources: *RHESSI* sees a hot and tenuous one, and AIA sees a cooler and denser one. Interestingly, the nonthermal energy
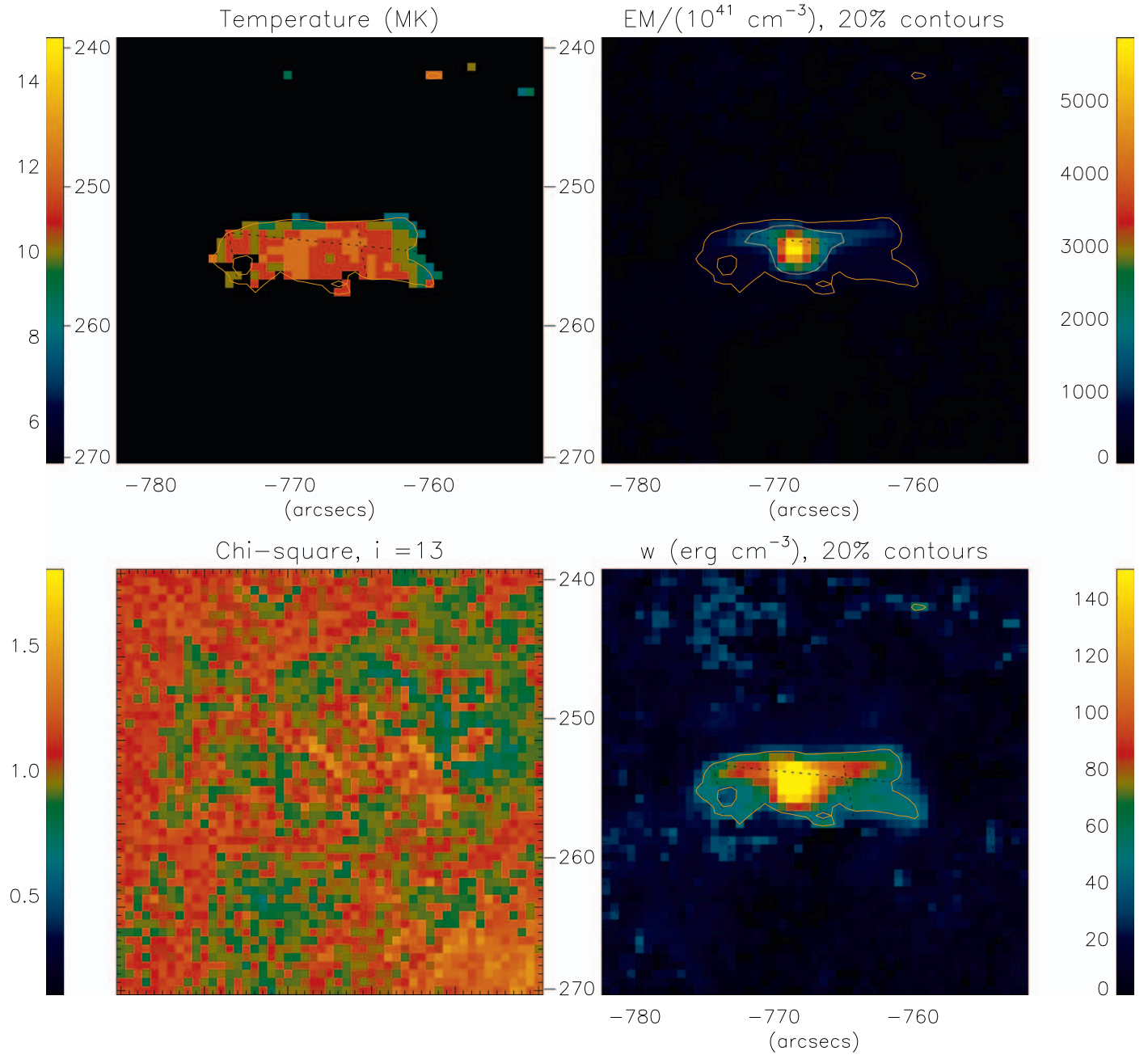
Figure 5. Temporal evolution of plasma parameters obtained with the regularized DEM maps derived from *SDO*/AIA data: maps of the mean temperature (top left), the emission measure (top right), chi-square (bottom left), and the thermal energy density (bottom right) for the 13th time interval (03:51:06–03:51:18 UT). The orange contour indicates 20% of the thermal energy density peak. The yellow contour indicates 20% of the emission measure peak. The mean temperature map is plotted only for pixels where the emission measure is greater than 5% of its maximum value for each time interval. An animation of this figure is available in the online Journal. The animation is the same as the static figure, but runs for all 41 time intervals, which is from 03:48:37 to 03:56:37 UT.

(An animation of this figure is available.)

(a blue histogram in Figure 6) is initially divided into roughly comparable portions between these two thermal sources. The sum of these two thermal energies roughly matches the available nonthermal energy deposition; thus the revealed evolution of various energy components is quantitatively consistent with the thermal energy being fully driven by the nonthermal energy deposition. No extra energy is needed to drive the observed plasma heating, while there is no unaccounted for nonthermal energy to drive any other form of energy, for example kinetic energy. Given that we do not see any eruptive activity associated with this flare, we have to

conclude that, in this flare, the free magnetic energy was primarily converted to nonthermal energy (acceleration of electrons), which, in its turn, was fully responsible for generation of the thermal energy component.

The hotter source seen by *RHESSI* cools more quickly than the other thermal source (Figure 4a). Thus, in the second stage, after ~03:51:46 UT, *RHESSI* started seeing the cooler and denser source—the same as AIA. The mismatch between the green and black curves in Figure 6 after 03:51:46 UT is about a factor of 2, which can be considered as a measure of uncertainty in defining the thermal energy by
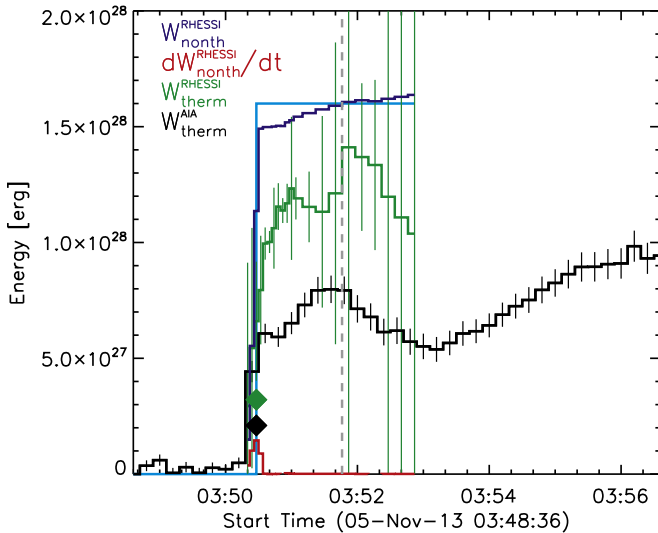
Figure 6. Evolution of energy components in the 2013 November 5 flare. The cumulative nonthermal energy deposition W_{nonth}^{RHESSI} obtained using parameters of the nonthermal part of the *RHESSI* fits (Equation (6)) is shown in blue. The thermal energy W_{therm}^{RHESSI} (Equation (7)) computed using the thermal part of the *RHESSI* fits is shown in green, while the thermal energy W_{therm}^{AIA} (Equation (10)) computed from the AIA DEM maps is shown in black. The red histogram shows the rate of *RHESSI* nonthermal energy deposition dW_{nonth}^{RHESSI}/dt [arbitrary units]. The vertical dashed line indicates the time 03:51:46 UT as in Figures 4(a) and (b). The green and black symbols indicate the model values of thermal energies for loops 1 and 2, respectively, for 03:50:28 UT; see Table 1. The light blue line shows the modeled total deposition of the nonthermal energy $\widetilde{W}$. For simplicity, the entire energy deposition is assigned here to the peak time of the impulsive phase.

two different instruments/techniques. Formally, due to its large statistical errors, the *RHESSI*-derived thermal energy is not significantly different from that derived from the AIA data after 03:51:46 UT, even though the mean values differ by a factor of 2. In addition to the statistical uncertainties, there are also noticeable systematic uncertainties, particularly because of poorly constrained volumes of the flaring loops. These uncertainties are difficult to firmly quantify; a reasonable ballpark estimate could be taken as a factor of 2, similar to the mismatch between the green and black curves after 03:51:46 UT.

3. Modeling of the 2013 November 5 Flare

To cross-check and validate our conclusions formulated above based mainly on analysis of EUV and X-ray data, and in particular to estimate how accurate our selection of the volume of the hot flaring loop seen by *RHESSI* was, we perform a 3D modeling and employ additional data: photospheric magnetograms, microwave images, and spectra. The 3D magnetic field model of the active region of interest is obtained using the automated model production pipeline (Nita et al. 2018) based on the NLFFF extrapolation code (Fleishman et al. 2017) initiated with the *SDO*/HMI (Scherrer et al. 2012) vector magnetogram (taken at 03:46:13.4 UT) that is used as the bottom boundary condition. Using the IDL-based simulation tool GX (Gyrosynchrotron/X-ray) simulator (Nita et al. 2015, 2018), we import the magnetic data cube, inspect the magnetic connectivity, and select two flux tubes roughly matching the available imaging data. These flux tubes are populated with thermal plasma and nonthermal electrons so as to match the available data for a single time (03:50:28 UT) near

the HXR peak as closely as possible (see an example of such a modeling performed by Kuroda et al. 2018, and references therein).

Once a model has been set up, GX Simulator permits microwave, X-ray, and EUV emission to be computed and compared with the observations. Recently, an ability to compute the thick-target X-ray emission has been added to GX Simulator, which now permits a much more realistic modeling of X-ray emission than was possible before. The mismatches between the simulated and observed data (both images and spectra) are removed by adjusting the spatial distributions of the thermal and nonthermal particles and other parameters of the adopted model such as density, temperature, and spectrum. Once the simulated emissions match the observations closely, the model is deemed validated.

Figure 7 shows the final validated model. Although both thermal plasma and nonthermal electrons are present in both model flaring loops, these loops make dissimilar contributions to emission in different domains. Flux tube 1 (Figure 7) is hotter and more tenuous, so it dominates the X-ray spectrum, though flux tube 2 (Figure 7) makes a non-negligible contribution to the X-ray emission. Flux tube 2 is cooler and denser; it dominates EUV emission detected by AIA. The two flux tubes contain comparable numbers of nonthermal electrons; however, given that the energy spectrum of the nonthermal electrons in flux tube 2 is noticeably harder than that in flux tube 1, flux tube 2 makes a dominant contribution to the microwave gyrosynchrotron emission. Individual contributions of our two flaring loops to the X-ray and microwave spectra are shown in Figure 8 by the dashed and dotted lines.

The solid curves in Figure 8 show a perfect match between simulated and observational spectral data in both X-ray and microwave domains. Comparison between the simulated and observed images requires additional co-alignment to make up for simulated image position errors. These errors originate from two sources. The first is a geometrical error due to projection effects (which is getting larger toward the limb) and also to distortions because of mismatch between the spherical shape of the Sun and the Cartesian coordinate system adopted for the modeling. The second source of error is an uncertainty in reproducing the magnetic field lines within the NLFFF data cube: on average the spatial deviation between the reconstructed and "true" field line has been estimated to be about 10% of the loop length (Fleishman et al. 2019).

In Section 2.1 we co-aligned the AIA images to match the *RHESSI* ones by adjusting the roll angle. Accordingly, here we co-align simulated X-ray images to match the observed *RHESSI* images by applying a shift of $dx = -1\rlap{.}''5, dy = -8\rlap{.}''6$ (Figure 9); the same shift was then applied to the simulated microwave images for consistency. This shift is in the range of the expected model positioning error described above.

Microwave images are obtained with NoRH, which itself might have a positioning error within $10''$ over both x and y coordinates; thus, the microwave images (see Figure 10) were further co-aligned with the (shifted) model images by shifting the observed ones by $dx = -3\rlap{.}''5, dy = -5\rlap{.}''7$ at 17 GHz, and by $dx = -5'', dy = 2''$ at 34 GHz, which is within the NoRH positioning accuracy.

These figures show a remarkable agreement between the simulated and observed spectra and images in both microwave and X-ray domains, and so validate the entire 3D model. This implies that the physical picture developed based on only a
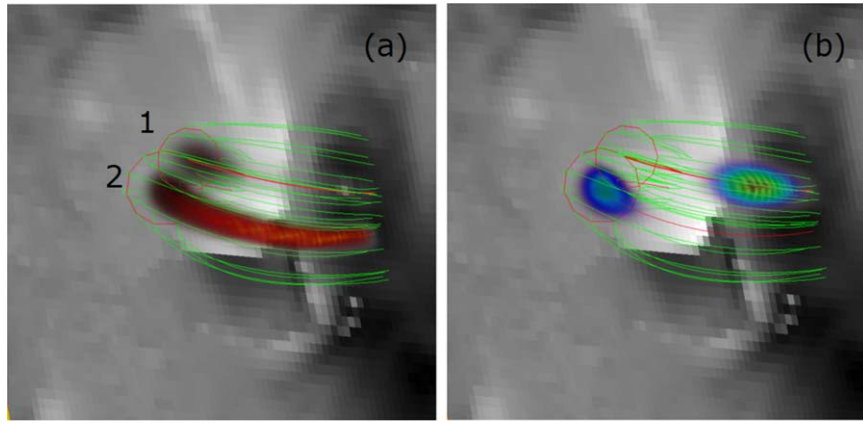
Figure 7. The 3D model with two flux tubes (closed loops) filled with thermal plasma (a) and nonthermal electrons (b) for the HXR impulse time (03:50:28 UT) overlaid on the LOS HMI magnetogram. Green lines visualize the closed field lines; the red lines and circles indicate corresponding central (reference) field lines and the cross-sectional areas of the flux tubes respectively. (a) The spatial distributions of thermal plasma in the flux tubes is shown by the red volume. The digits indicate flux tubes 1 and 2. (b) The spatial distribution of nonthermal electrons in two flux tubes is shown by the blue–green volume.

subset of available data, namely in EUV and X-rays, is also consistent with data from other contexts—photospheric magnetic field measurements and microwave imaging and spectroscopy; thus, it captures at least the main flare properties and so can be conclusively used to quantify this flare in 3D.

Using the model, validated by comparison between simulated and observed emissions, we cross-check our assumptions and findings derived from the data analysis. The most relevant numbers of the model are summarized in Table 1. In Section 2.2, we adopted that both flux tubes have the same volume. In the model, their volumes are indeed comparable, although not identical: they differ almost by a factor of 3, which validates our assumptions within the same factor for the volume itself and within a factor of $\sim\sqrt{3}$ for the energy.

Let us now evaluate whether the amount of nonthermal energy in the model is sufficient to supply the observed thermal energy in both loops. The model contains instantly $\sim 4 \times 10^{26}$ erg of the total nonthermal energy, which is divided roughly equally between these two loops. To estimate the total deposition of the nonthermal energy $\widetilde{W}$, we have to estimate the escape time τ of the nonthermal electrons from the loops and the total duration of the nonthermal energy injection Δt (at the level of half maximum): $\widetilde{W} \approx \Delta t W_{nth}/\tau$. To estimate the escape time, we suppose that the nonthermal electrons escape the loops more or less freely, such as $\tau \sim l/v \sim 0.2$–0.3 s, where $l \approx 1.5 \times 10^9$ cm (see Table 1) for any of the loops and $v \approx 0.2c$ is the velocity of 10 keV electrons. From the full duration of the nonthermal X-ray and radio emission, ≈ 15 s, we find $\Delta t \approx 8$ s. Putting all numbers together, we obtain $\widetilde{W} \approx 1.6 \times 10^{28}$ erg (Figure 6, light blue line), in perfect agreement with the nonthermal energy deposition derived from the X-ray data analysis (Figure 6, dark blue line). The thermal energies of both flaring loops are obtained by direct integration over the model volume within the GX Simulator tool. They are shown by green and black symbols in Figure 6 and match well those derived from the data. Thus, our data-constrained and data-validated 3D model agrees well with the results of the data analysis performed in Section 2.

4. Discussion and Conclusions

Veronig et al. (2005) proposed to distinguish between the "empirical Neupert effect" (ENE) and the "theoretical Neupert effect" (TNE), where ENE refers to relationships between the observed thermal and nonthermal *emissions*, while TNE refers to the inferred thermal and nonthermal *energies*. In contrast to their expectation, however, Veronig et al. (2005) found that ENE shows a noticeably higher statistical significance than TNE. Two main sources of the lower significance of TNE were proposed: (i) the potential presence of additional plasma heating unrelated to the nonthermal electron loss and (ii) uncertainty in quantification of the nonthermal energy related primarily to the uncertainty of the low-energy cutoff in the spectrum of flare-accelerated electrons used to derive the X-ray thick-target spectral fit. Therefore, to quantify the TNE much more conclusively requires that those two uncertainties have been removed or at least minimized. This requirement is well fulfilled for the "cold" flares (Lysenko et al. 2018). Indeed, these flares show the weakest thermal response of any flares, show no "direct" preflare heating, and their nonthermal X-ray emission dominates down to unusually low energies, enabling the low-energy cutoff values to be recovered a factor of a few lower than in an average flare. In addition, the low-energy cutoff can now be much better constrained using a recently developed warm-target fit (Kontar et al. 2019).

In this paper we have performed a detailed analysis of one "cold" flare, SOL2013-11-05T035054, which is ideal for such a case study because in addition to the mentioned advantages common to all flares from this subclass, it was observed with a combination of instruments sensitive to the nonthermal component as well as both hot and warm plasma. Furthermore, the flare displayed a simple single rise-and-fall time profile, which simplifies analysis of the evolution of the energy component enormously compared with flares having complex light curves.

We have found that morphologically the flare consisted of two reasonably compact flux tubes, where a single episode of electron acceleration happened. Thus, the release of flaring energy is likely driven by inductive interaction resulting in magnetic reconnection between these two flux tubes. The accelerated nonthermal electrons have their energy roughly equally between these two flaring loops. However, the spectral slopes of these two nonthermal electron populations are different from each other: it is harder in cooler loop 2 than in hot loop 1 (see Table 1). Although we cannot nail down the exact reason for that, we believe that some sort of
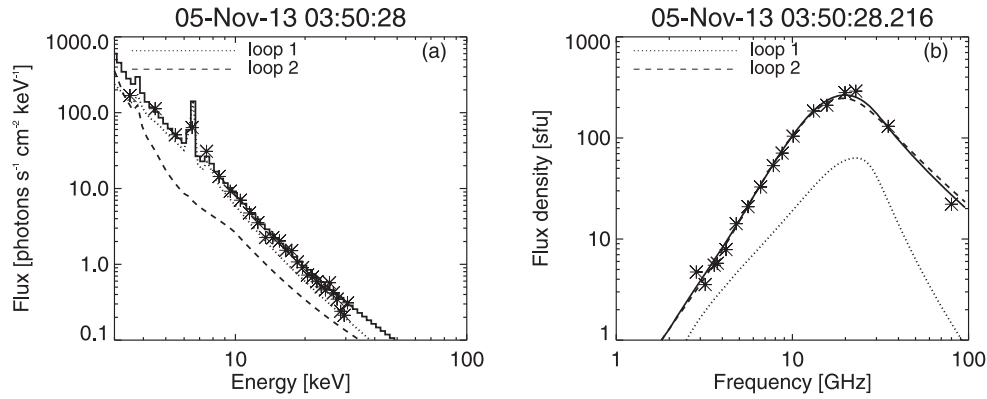
Figure 8. (a) The observed *RHESSI* X-ray spectrum for the time interval 03:50:28–03:50:32 UT (asterisks) and the corresponding simulated spectrum (histogram) from the 3D model; (b) the same for the radio domain with NoRP and SRS data at 03:50:28 UT (asterisks) and the simulated microwave spectrum (black solid line). The dotted and dashed lines correspond to contributions from loop 1 and loop 2 separately to the X-ray and the radio simulated spectra.

energy-dependent electron transport from the acceleration region to the loops must be involved, perhaps due to wave–particle interactions.

It is further interesting that in spite of comparable amounts of nonthermal energy deposited in both these loops (resulting in comparable amounts of thermal energy), their specific thermal responses are rather dissimilar. Indeed, one loop remained tenuous with only a modest increase in EM but became hot with a temperature up to ∼30 MK (that seen by *RHESSI*); the other one displayed a larger EM, but was heated more gently (only up to ∼10 MK). In the course of the flare, the hotter and more tenuous flux tube experienced a faster cooling (in agreement with the anticipated faster rate of heat conduction); thus, the cooler flux tube survived longer and dominated the late phase of the post-flare cooling.

It is puzzling why these two flux tubes react that differently in response to comparable impacts from nonthermal electrons. There could be several possible causes; however, it is difficult to understand within the chromospheric evaporation alone without considering nonthermal electron loss in the coronal portion of the flaring loops. First, the spectral slopes of the nonthermal electrons are different in these two loops (see Table 1). Simulations of the chromospheric response in flaring loops (Nagai & Emslie 1984; Fisher et al. 1985; Mariska et al. 1989; Reep et al. 2015) do show a dependence of the response on the spectral slope: softer nonthermal spectra yield more efficient evaporation as they deposit their nonthermal energy higher in the chromosphere. However, in our case, we see exactly the opposite trend: the loop with softer nonthermal spectrum remains more tenuous. Second, the energy deposited into the chromospheric footpoints depends on the flux tube geometry, and in particular on the footpoint area, which itself depends on the mirror ratio of the loop. Interestingly, within our 3D model, the two flaring loops have comparable mirror ratios of about 3, which does not favor one loop over the other in terms of nonthermal electron precipitation to the footpoints. Third, a beam-like pitch-angle anisotropy, if present, may enhance the precipitation. Again, we do not see any evidence in favor of that: the footpoint HXR source in loop 1 is stronger than that in loop 2, which implies that the nonthermal electron precipitation was stronger in the tenuous loop (loop 1). This implies that the chromospheric evaporation took place in loop 1, while working in a regime of only a modest enhancement of the coronal plasma density, but efficient heating. Most likely, loop 2 was denser from the beginning, so the lowest-energy

nonthermal electrons lost their energy in the coronal portion of loop 2, thus providing a modest heating of this plasma, while the chromospheric evaporation was driven by less numerous higher-energy electrons, resulting in a more gentle evaporation. A combination of these two processes likely resulted in a cooler and denser plasma in loop 2 than loop 1.

It is remarkable that the nonthermal energy deposition (∼1.5×10^{28} erg) over the impulsive flare phase matches nicely the sum of the thermal energies of the two flaring flux tubes (∼1×10^{28} erg in the hotter one and ∼0.5×10^{28} erg in the cooler one). This implies that, within the uncertainties, the observed thermal energy is entirely supplied by the nonthermal electrons, i.e., it displays a clear picture of the TNE. There is no statistically significant room for other sources of energy (e.g., direct heating or acceleration of ions), which would drive extra heating and evaporation. Similarly, there is no indication of any other secondary energies (rather than the thermal one), such as kinetic energy of regular motion (e.g., an eruption).

Appendix
Statistical Uncertainties of the Involved Parameters

Both OSPEX and regularized inversion provide statistical errors of the output parameters. In this paper, however, we use a number of measures constructed from a combination of the immediate outcomes of the codes, such as the energy densities, whose statistical uncertainties must be computed from the error propagation.

To compute the statistical uncertainty of the EM obtained from DEM distribution using Equation (1), we note that the DEMs there can each be expressed as a sum of a mean component $\overline{\xi_i(T_i)}$ and a fluctuating component $\delta\xi_i(T_i)$: $\xi_i(T_i) = \overline{\xi_i(T_i)} + \delta\xi_i(T_i)$, and we assume that the fluctuating components are not correlated with each other so that $\langle\delta\xi_i\delta\xi_j\rangle = 0$ for $i \neq j$. In this case we can compute the
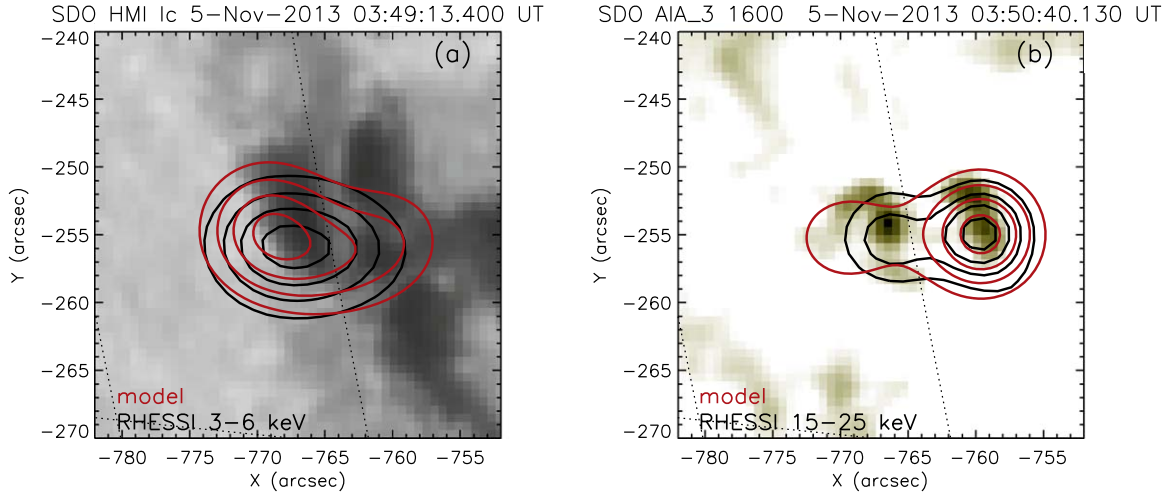
Figure 9. The *RHESSI* CLEAN 3–6 keV (a) and 15–25 keV (b) 30%, 50%, 70%, and 90% contours (black lines) and point spread function (PSF)-convolved model image contours (red lines) for the same energies for the time interval 03:50:20–03:50:40 UT overlaid on (a) an *SDO*/HMI white-light image and (b) the AIA map in the 1600 Å wavelength channel. To co-align the *RHESSI* and HMI maps the HMI roll angle has been changed in a similar way to the AIA map: HMI_roll_angle = 0.11. For co-alignment of the model X-ray images and the *RHESSI* images a shift of $dx = -1\rlap{.}''5$, $dy = -8\rlap{.}''6$ has been applied to the simulated images as explained in the text.

standard deviation of a sum $g = \sum_{i=1}^{N} g_i$ of uncorrelated variables g_i from their standard deviations δg_i as

$$\delta g = \sqrt{\sum_{i=1}^{N} (\delta g_i)^2}, \quad (11)$$

which, being applied to Equation (1), yields

$$\delta \mathrm{EM}_{\mathrm{AIA}} = A \sqrt{\sum_i \overline{\delta \xi_i^2}(T_i) \Delta T_i^2}, \quad (12)$$

where $\overline{\delta \xi_i}(T_i)$ are the DEM errors for temperatures T_i in the range 0.5–25 MK, obtained from the regularization method by Hannah & Kontar (2012, 2013).

The temperature $\langle T_{\mathrm{AIA}} \rangle$ defined by Equation (2) is a ratio of two values that both contain uncertainties. In this case it is convenient to use a general equation for the (independent) error propagation,

$$\delta f = \sqrt{\left(\frac{\partial f}{\partial x}\right)^2 \delta_x^2 + \left(\frac{\partial f}{\partial y}\right)^2 \delta_y^2}, \quad (13)$$

where δ_x and δ_y represent the standard deviations of the random x and y values, respectively, which, being applied to Equation (2), yields

$$\delta \langle T_{\mathrm{AIA}} \rangle = \sqrt{\frac{A^2}{\mathrm{EM}_{\mathrm{AIA}}^2} \sum_i T_i^2 \overline{\delta \xi_i^2}(T_i) \Delta T_i^2 + \frac{\langle T_{\mathrm{AIA}} \rangle^2}{\mathrm{EM}_{\mathrm{AIA}}^2} \delta \mathrm{EM}_{\mathrm{AIA}}^2}. \quad (14)$$

Similar equations are valid for the emission measure and the temperature defined for individual pixels from the DEM maps, Equations (3) and (4).

The statistical errors of the thermal energy density defined by Equation (5) from the AIA data can also be computed following Equation (13) from the standard deviations of

$\mathrm{EM}_{ij}^{\mathrm{AIA}}$ and $\langle T_{ij}^{\mathrm{AIA}} \rangle$:

$$\delta w_{ij}^{\mathrm{AIA}} = \sqrt{\left(\frac{\partial w_{ij}^{\mathrm{AIA}}}{\partial \langle T_{ij}^{\mathrm{AIA}} \rangle}\right)^2 (\delta \langle T_{ij}^{\mathrm{AIA}} \rangle)^2 + \left(\frac{\partial w_{ij}^{\mathrm{AIA}}}{\partial \mathrm{EM}_{ij}^{\mathrm{AIA}}}\right)^2 (\delta \mathrm{EM}_{ij}^{\mathrm{AIA}})^2}, \quad (15)$$

where $\partial w_{ij}^{\mathrm{AIA}} / \partial \mathrm{EM}_{ij}^{\mathrm{AIA}} = 3 k_{\mathrm{B}} (S_{\mathrm{px}} \, l_{\mathrm{depth}})^{-0.5} \langle T_{ij}^{\mathrm{AIA}} \rangle / (2 \sqrt{\mathrm{EM}_{ij}^{\mathrm{AIA}}})$ and $\partial w_{ij}^{\mathrm{AIA}} / \partial \langle T_{ij}^{\mathrm{AIA}} \rangle = 3 k_{\mathrm{B}} (S_{\mathrm{px}} \, l_{\mathrm{depth}})^{-0.5} \sqrt{\mathrm{EM}_{ij}^{\mathrm{AIA}}}$. Substitution of these derivatives into Equation (15) yields

$$\delta w_{ij}^{\mathrm{AIA}} = 3 k_{\mathrm{B}} (S_{\mathrm{px}} \, l_{\mathrm{depth}})^{-0.5}$$
$$\times \sqrt{\mathrm{EM}_{ij}^{\mathrm{AIA}} (\delta \langle T_{ij}^{\mathrm{AIA}} \rangle)^2 + \frac{(\langle T_{ij}^{\mathrm{AIA}} \rangle)^2}{4 \mathrm{EM}_{ij}^{\mathrm{AIA}}} (\delta \mathrm{EM}_{ij}^{\mathrm{AIA}})^2}. \quad (16)$$

Finally using Equation (11) the uncertainties on the total thermal energy (see Equation (10)) of the FOV AIA data are

$$\delta W_{\mathrm{therm}}^{\mathrm{AIA}} = S_{\mathrm{px}} \, l_{\mathrm{depth}} \sqrt{\sum_{i=1}^{N_{\mathrm{px}}} \sum_{j=1}^{N_{\mathrm{px}}} (\delta w_{ij}^{\mathrm{AIA}})^2}. \quad (17)$$

The same approach was used in the calculation of the uncertainties on the thermal energy (see Equation (7)) detected by *RHESSI*:

$$\delta W_{\mathrm{therm}}^{\mathrm{RHESSI}} = 3 k_{\mathrm{B}} \sqrt{V}$$
$$\times \sqrt{\mathrm{EM}_{\mathrm{RHESSI}} \delta T_{\mathrm{RHESSI}}^2 + \frac{T_{\mathrm{RHESSI}}^2}{4 \mathrm{EM}_{\mathrm{RHESSI}}} \delta \mathrm{EM}_{\mathrm{RHESSI}}^2}, \quad (18)$$

where $\delta \mathrm{EM}_{\mathrm{RHESSI}}$ and $\delta T_{\mathrm{RHESSI}}$ are the errors on the *RHESSI* best-fit parameters and are returned by OSPEX[7] and based on the curvature matrix in parameter space.

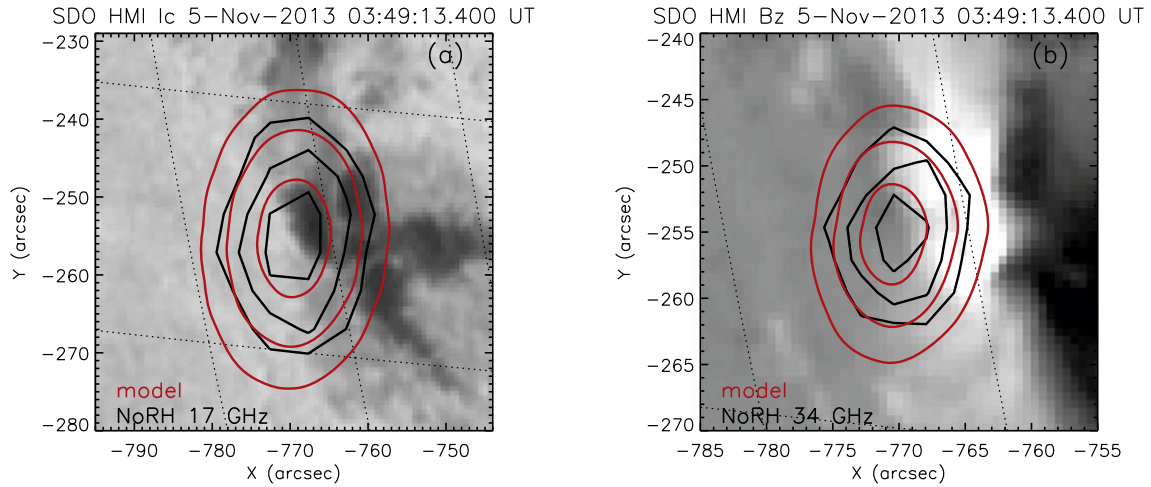[7] https://hesperia.gsfc.nasa.gov/ssw/packages/spex/doc/ospex_explanation.htm

Figure 10. The NoRH 17 GHz (a) and 34 GHz (b) 50%, 70%, and 90% contours (black lines) and PSF-convolved model image contours (red lines) at the same frequencies overlaid on an *SDO*/HMI white-light image (a) and LOS magnetogram (b). To co-align the images we applied: (i) HMI_roll_angle = 0.11 as for AIA images; (ii) a shift of $dx = -1{.}''5$, $dy = -8{.}''6$ to the model images following Figure 9; (iii) a shift of $dx = -3{.}''5$, $dy = -5{.}''7$ for the NoRH 17 GHz image and $dx = -5''$, $dy = 2''$ for the 34 GHz NoRH image.

Table 1
Summary of the 3D Model

Parameter	Symbol, units	Loop 1	Loop 2
Geometry:			
Length of the central field line	l, cm	1.46×10^9	1.62×10^9
Model volume; $\left[\int n_0 dV\right]^2 / \int n_0^2 dV$	V, cm^3	6.86×10^{25}	2.39×10^{25}
Thermal plasma:			
Emission measure, $\int n_0^2 dV$	EM, cm^{-3}	1.40×10^{45}	1.69×10^{46}
Mean number density, $\int n_0^2 dV / \int n_0 dV$	$n_{\rm th}$, cm^{-3}	0.45×10^{10}	2.66×10^{10}
Temperature	T, MK	25	8
Instant total thermal energy	$W_{\rm th}$, erg	3.21×10^{27}	2.1×10^{27}
Nonthermal electrons:			
Total electron number	N_b, cm^{-3}	8.1×10^{33}	7×10^{33}
Low-energy cutoff	E_0, keV	10	10
Spectral index	δ	4.3	3.3
Instant total nonthermal energy	$W_{\rm nth}$, erg	1.85×10^{26}	2×10^{26}

ORCID iDs

Galina G. Motorina ⓘ https://orcid.org/0000-0001-7856-084X
Gregory D. Fleishman ⓘ https://orcid.org/0000-0001-5557-2100
Eduard P. Kontar ⓘ https://orcid.org/0000-0002-8078-0902

References

Altyntsev, A. A., Fleishman, G. D., Lesovoi, S. V., & Meshalkina, N. S. 2012, ApJ, 758, 138
Altyntsev, A. T., Meshalkina, N. S., Lysenko, A. L., & Fleishman, G. D. 2019, ApJ, 883, 38
Aptekar, R. L., Frederiks, D. D., Golenetskii, S. V., et al. 1995, SSRv, 71, 265
Bastian, T. S., Fleishman, G. D., & Gary, D. E. 2007, ApJ, 666, 1256
Battaglia, M., Fletcher, L., & Benz, A. O. 2009, A&A, 498, 891
Battaglia, M., & Kontar, E. P. 2011, A&A, 533, L2
Battaglia, M., Kontar, E. P., & Motorina, G. 2019, ApJ, 872, 204
Battaglia, M., Motorina, G., & Kontar, E. P. 2015, ApJ, 815, 73
Bian, N. H., Kontar, E. P., & Emslie, A. G. 2016, ApJ, 824, 78
Bogachev, S. A., & Somov, B. V. 2005, AstL, 31, 537
Brown, J. C., & Hoyng, P. 1975, ApJ, 200, 734
Carmichael, H. 1964, NASSP, 50, 451
Chupp, E. L. 1996, in AIP Conf. Ser. 374, ed. R. Ramaty, N. Mandzhavidze, & X.-M. Hua (New York: AIP), 3
Dahlin, J. T., Drake, J. F., & Swisdak, M. 2017, PhPl, 24, 092110
Datlowe, D. W. 1975, in IAU Symp. 68, Solar Gamma-, X-, and EUV Radiation, ed. S. R. Kane (Dordrecht: Reidel), 191
Dennis, B. R. 1985, SoPh, 100, 465
Dennis, B. R., & Zarro, D. M. 1993, SoPh, 146, 177
Feldman, U., Hiei, E., Phillips, K. J. H., Brown, C. M., & Lang, J. 1994, ApJ, 421, 843
Fisher, G. H., Canfield, R. C., & McClymont, A. N. 1985, ApJ, 289, 414
Fleishman, G., Mysh'yakov, I., Stupishin, A., Loukitcheva, M., & Anfinogentov, S. 2019, ApJ, 870, 101
Fleishman, G. D., Anfinogentov, S., Loukitcheva, M., Mysh'yakov, I., & Stupishin, A. 2017, ApJ, 839, 30
Fleishman, G. D., Kontar, E. P., Nita, G. M., & Gary, D. E. 2011, ApJL, 731, L19
Fleishman, G. D., Nita, G. M., & Gary, D. E. 2015, ApJ, 802, 122
Fleishman, G. D., Pal'shin, V. D., Meshalkina, N., et al. 2016, ApJ, 822, 71
Gary, D. E., & Hurford, G. J. 1989, ApJ, 339, 1115
Grady, K. J., Neukirch, T., & Giuliani, P. 2012, A&A, 546, A85
Guidice, D. A., Cliver, E. W., Barron, W. R., & Kahler, S. 1981, BAAS, 13, 553
Hanaoka, Y. 1999, PASJ, 51, 483
Hannah, I. G., & Kontar, E. P. 2012, A&A, 539, A146
Hannah, I. G., & Kontar, E. P. 2013, A&A, 553, A10
Hirayama, T. 1974, SoPh, 34, 323
Holman, G. D., Aschwanden, M. J., Aurass, H., et al. 2011, SSRv, 159, 107
Hurford, G. J., Schmahl, E. J., Schwartz, R. A., et al. 2002, SoPh, 210, 61
Jakimiec, J., & Fludra, A. 1991, AdSpR, 11, 99
Jakimiec, J., Tomczak, M., Falewicz, R., Phillips, K. J. H., & Fludra, A. 1998, A&A, 334, 1112
Kašparová, J., Karlický, M., Kontar, E. P., Schwartz, R. A., & Dennis, B. R. 2005, SoPh, 232, 63
Kontar, E. P., Hannah, I. G., Jeffrey, N. L. S., & Battaglia, M. 2010, ApJ, 717, 250
Kontar, E. P., Jeffrey, N. L. S., & Emslie, A. G. 2019, ApJ, 871, 225
Kopp, R. A., & Pneuman, G. W. 1976, SoPh, 50, 85
Krucker, S., Hudson, H. S., Glesener, L., et al. 2010, ApJ, 714, 1108
Kuhar, M., Krucker, S., Martínez Oliveros, J. C., et al. 2016, ApJ, 816, 6
Kuroda, N., Gary, D. E., Wang, H., et al. 2018, ApJ, 852, 32
Lemen, J. R., Title, A. M., Akin, D. J., et al. 2012, SoPh, 275, 17
Lin, R. P., Dennis, B. R., Hurford, G. J., et al. 2002, SoPh, 210, 3
Lysenko, A. L., Altyntsev, A. T., Meshalkina, N. S., Zhdanov, D., & Fleishman, G. D. 2018, ApJ, 856, 111
Mariska, J. T., Emslie, A. G., & Li, P. 1989, ApJ, 341, 1067
Masuda, S., Shimojo, M., Kawate, T., Ishikawa, S.-n., & Ohno, M. 2013, PASJ, 65, S1
McTiernan, J. M., Fisher, G. H., & Li, P. 1999, ApJ, 514, 472

Miller, J. A., Guessoum, N., & Ramaty, R. 1990, ApJ, 361, 701
Motorina, G. G., & Kontar, E. P. 2015, Ge&Ae, 55, 995
Muratov, A. A. 2011, in 12th Conference of Young Scientists, Vol. 365, Baikal
    Young Scientists' International School, 85, http://ckm.iszf.irk.ru/images/
    2011/Sbornik-2011/Section-A/Muratov-85-87.pdf
Nagai, F., & Emslie, A. G. 1984, ApJ, 279, 896
Neupert, W. M. 1968, ApJL, 153, L59
Nita, G. M., Fleishman, G. D., Kuznetsov, A. A., Kontar, E. P., & Gary, D. E.
    2015, ApJ, 799, 236
Nita, G. M., Viall, N. M., Klimchuk, J. A., et al. 2018, ApJ, 853, 66
Pal'shin, V. D., Charikov, Y. E., Aptekar, R. L., et al. 2014, Ge&Ae, 54, 943
Priest, E. R., & Forbes, T. G. 2002, A&ARv, 10, 313
Reep, J. W., Bradshaw, S. J., & Alexander, D. 2015, ApJ, 808, 177
Sakurai, K. 1965, PASJ, 17, 403
Scherrer, P. H., Schou, J., Bush, R. I., et al. 2012, SoPh, 275, 207

Shibata, K. 1999, Ap&SS, 264, 129
Shibata, K., Masuda, S., Shimojo, M., et al. 1995, ApJL, 451, L83
Somov, B. V. 1979, SvAL, 5, 28
Stepanov, A. V., & Zaitsev, V. V. 2016, Ge&Ae, 56, 952
Sturrock, P. A. 1966, Natur, 211, 695
Su, Y., Gan, W. Q., & Li, Y. P. 2008, AdSpR, 41, 988
Sui, L., Holman, G. D., & Dennis, B. R. 2007, ApJ, 670, 862
Sylwester, B., Sylwester, J., Serio, S., et al. 1993, A&A, 267, 586
Tajima, T., Sakai, J., Nakajima, H., et al. 1987, ApJ, 321, 1031
Torii, C., Tsukiji, Y., Kobayashi, S., et al. 1979, PRIAN, 26, 129
Tsuneta, S. 1997, ApJ, 483, 507
Veronig, A. M., Brown, J. C., Dennis, B. R., et al. 2005, ApJ, 621, 482
White, S. M., Kundu, M. R., Bastian, T. S., et al. 1992, ApJ, 384, 656
White, S. M., Thomas, R. J., & Schwartz, R. A. 2005, SoPh, 227, 231
Zaitsev, V. V., & Stepanov, A. V. 2017, SoPh, 292, 141